ORIGINAL RESEARCH **Open access**

Toward Precision Viticulture: UAV and Mobile Robot-Based Assessment of Vineyard Water Status

Aisha Bello[1*], Zainab Sule[1], Ibrahim Musa[2], Grace Adeyemi[3], Ahmed Youssef[4]

Abstract

In this paper, we introduce an innovative technique to investigate how water regimes influence grapevine canopy conditions, leveraging robotics to facilitate monitoring and spatial mapping. Multispectral imagery, along with several vegetation indices, is acquired using an unmanned aerial vehicle (UAV), whereas a ground-based mobile robot delivers the 3D canopy reconstruction. Unlike prior research, 60 vegetation indices are calculated with high accuracy by using the projected area of the vineyard point cloud as a mask. Thorough experimental evaluations on replicated Pinot gris vine plots reveal strong positive correlations between the GDVI, PVI, and TGI vegetation indexes and water potential: GDVI (R2=0.90 and 0.57 for stem and pre-dawn water potential, respectively), PVI (R2=0.90 and 0.57), TGI (R2=0.87 and 0.77). In addition, canopy volume and ground-projected canopy area respond to variations in water status, as do stem and pre-dawn water potential measurements. The outcomes of this research validate the practicality of the proposed method and underscore the promising role of robotic systems in precision viticulture.

Keywords Vegetation indexes, Robotics, Precision viticulture, Water potential, 3D reconstruction

*Correspondence:
Aisha Bello
aisha.bello@ui.edu.ng
[1] Department of AI for Cowpea and Groundnut Aflatoxin Risk Prediction, Faculty of Agriculture, University of Ibadan, Ibadan, Nigeria
[2] Department of Smart Post-Harvest Handling and Drying Analytics, Faculty of Agriculture, University of Ilorin, Ilorin, Nigeria
[3] Department of Machine Learning for Storage Pest Detection, Faculty of Agriculture, Federal University of Agriculture Abeokuta, Abeokuta, Nigeria
[4] Department of Precision Storage Temperature Control, Faculty of Agriculture, University of Khartoum, Khartoum, Sudan

Introduction

In recent times, global warming has intensified droughts in agriculture, posing serious threats to plant survival and worldwide food production [1]. In the near future, extreme drought episodes are anticipated to increase in frequency, according to reports from the Intergovernmental Panel on Climate Change of the United Nations [2]. Furthermore, rising temperatures linked to climate change will increase the evaporative demand on both plants and soil, increasing the likelihood of water stress across various crops [3]. Concurrently, the growing global population is expected to drive higher food requirements, while insufficient water resources will hinder adequate food production [4].

Plants employ multiple adaptive strategies to handle water stress [5]. Typically, they limit growth and close stomata to curb transpiration losses, which in turn reduces photosynthetic activity [6]. Water stress leads to smaller leaves, thereby reducing overall leaf area and canopy volume [7]. In specific scenarios, controlled moderate water stress can promote greater drought resistance, improved yields, and enhanced physiological performance [8]. However, severe water stress risks plant survival by depleting stored reserves and causing hydraulic dysfunction [9].

This is an open access article distributed under the terms of the Creative Commons Attribution-NonCommercial-ShareAlike 4.0 International License (CC BY-NC-SA 4.0), which permits non-commercial use, distribution, reproduction, and adaptation in any medium or format, provided that appropriate credit is given to the original author(s) and source, a link to the license is provided, and any changes made are indicated. Adapted material must be distributed under the same license.

© 2025 The Author(s). | Published by Agro Intelligence Research Press

Plant water status is commonly evaluated using several indicators, among which water potential is the most widely used traditional approach. Nevertheless, this method is destructive, necessitates extensive sampling within each plot, and is confined to limited time periods (generally from 12 noon to 3 p.m., or before sunrise) [10]. Various water potential metrics serve different goals. For instance, stem water potential is widely used to identify water stress [11], while pre-dawn water potential serves as an estimate of soil water potential [12].

Alternative assessments, including stomatal conductance, demand even greater complexity due to specialized equipment and calibration needs [10]. Moreover, traditional water stress monitoring overlooks variability in plants and soil, and field-based automation of actual evapotranspiration remains undeveloped [13]. Hence, interest is growing in accessible new techniques for tracking plant condition dynamically across space and time [14, 15] — for example, via multispectral imaging [16, 17] and structural metrics such as canopy surface area and volume [18].

Unmanned aerial vehicles (UAVs) equipped with spectral cameras provide georeferenced, high-resolution spectral data at moderate cost [17, 19]. Yet, UAV multispectral outputs can be influenced by surrounding factors, such as ground reflectance, weather patterns, soil moisture levels, and sensor properties, which all modify field spectral behavior [19, 20]. Over the decades, researchers have developed over 100 vegetation indices (VIs) from standard multispectral bands to reduce the impact of these external variables [21].

Additionally, canopy condition assessment benefits from dimensional parameters (such as height and volume) extracted through 3D point cloud analysis [22]. Comparative studies demonstrate that ground-based mapping systems yield more precise geometric data than UAV platforms [23]. Within this framework, mobile robotics paired with remote sensing offers significant value for crop monitoring and mapping [24]. Compared with UAVs, ground robots support larger payloads, closer observation distances, and denser point clouds [25]. They also deliver better operational flexibility, ground-level interaction capabilities, and reduced sensitivity to adverse weather.

The scientific literature contains multiple cases of mobile robots using onboard Light Detection and Ranging (LiDAR) sensors to build three-dimensional plant and crop maps [26], benefiting from extended range, rapid scanning, and lighting independence. For improved 3D reconstruction, 2D LiDAR units are often aligned with the laser plane perpendicular to the robot's direction of travel [27, 28]. One such application involves a custom robot with a height-adjustable 2D LiDAR mast for vineyard mapping [29]. In another case, a 2D LiDAR mounted on an all-terrain vehicle was used to scan an olive grove [30]. 3D LiDAR sensors represent a superior choice, providing broader coverage and dense environmental point clouds directly, despite potentially lower resolution than 2D systems [24, 31]. Their main shortcoming in horticultural settings occurs during rainfall, when raindrops scatter laser beams, resulting in unreliable point clouds [32].

Today, 3D point cloud generation of environments commonly relies on Simultaneous Localization and Mapping (SLAM) techniques that combine sequential scans. However, SLAM outputs are mostly utilized for robot navigation. As an alternative, structure-from-motion (SfM) methods reconstruct surroundings from image sequences captured at multiple positions [33] or through externally calibrated multi-camera setups [34]. Still, SfM reconstructions remain vulnerable to small movements of vegetation, such as wind-induced leaf motion.

Repetitive environments can challenge LiDAR-based SLAM performance. For this reason, modern SLAM solutions frequently incorporate sensor fusion with georeferencing data [35]. Examples include LiDAR-IMU fusion tested in vineyards [18] and LiDAR-GNSS integration for more robust positioning [36].

Once a 3D point cloud is established, geometric properties can be derived by partitioning the map into uniform grids and aggregating voxel volumes [29], or by generating enclosing meshes via triangulation methods such as Convex Hull [31] or Alpha Shape [18].

The literature also presents geometric maps from mobile robots, enriched with spectral information (e.g., NDVI and NDRE) collected by onboard cameras. A mobile robot carrying RGB, multispectral, and hyperspectral cameras produced

© 2025 The Author(s). | Published by Agro Intelligence Research Press

an NDVI map of a horticultural area in Cubero *et al.* [37]. Comparable NDVI mosaics for red cabbage rows were developed in Ulloa *et al.* [38]. Lateral positioning of spectral sensors proves effective for row-planted crops [39, 40]. Specific systems combining 2D LiDAR with Optrx Crop sensors for simultaneous volume reconstruction and NDVI mapping are reported in Bietresato *et al.* [41] and Ristorto *et al.* [42].

Photogrammetry also enables the creation of 3D multispectral point clouds [43-45]. Thermal point clouds have been generated using combined RGB-thermal imagery [46, 47] or thermal-LiDAR data fusion for crop observation [48].

Data fusion between targeted ground robot surveys and aerial platforms exploits complementary viewpoints and scales, as shown in several works [25, 31, 49-51]. However, detailed evaluations of this dual-platform integration remain scarce. A direct comparison of 3D point clouds from the Thorvald robot versus UAV orthomosaics is available in Tagarakis *et al.* [52]. In Pretto *et al.* [53], UAV-derived large-scale models were improved with fine-grained mobile robot data. In Zhang *et al.* [54], UAV and ground RGB images were merged to enable detailed intra-tree analysis, overcoming occlusions and adapting to variations in vertical canopy density.

Concerning water status assessment, 3D imaging for drought evaluation was explored in Briglia *et al.* [55]. Thermal infrared imagery combined with stereovision was used to analyze potato water stress in Wang *et al.* [47]. Automated 3D phenotyping for early water-stress detection was proposed by Rossi *et al.* [56]. Nevertheless, to date, no prior work has examined the impacts of the water regime on the grapevine canopy using combined UAV and mobile robot data.

In this study, we develop a new methodology to analyze how varying water regimes affect water potential, vegetation indices, and geometric features of grapevine canopies. This is realized by merging mobile robot geometric data with UAV spectral information and standard field measurements (stem and pre-dawn water potential). The core contribution lies in coupling UAV and robot datasets to isolate spectral signals strictly to canopy elements, thereby excluding extraneous surfaces.

Materials and Methods

Vineyard site and experimental design

Experiments were carried out during 2022 inside a vineyard managed by the University of Udine (North Eastern Italy, Lat. 46°01’53.0” N, Long. 13°13’29.0” E, 113 m above sea level). This vineyard, established in 2013, included Pinot gris clone R6 vines grafted on SO4 rootstock at a density of 4000 plants/ha (1.0 m between vines × 2.5 m between rows) and incorporated a sub-irrigation setup **(Figure 1)**. The vines followed a single guyot training system. They grew in gravely loam soil notable for its solid organic matter levels.

© 2025 The Author(s). | Published by Agro Intelligence Research Press

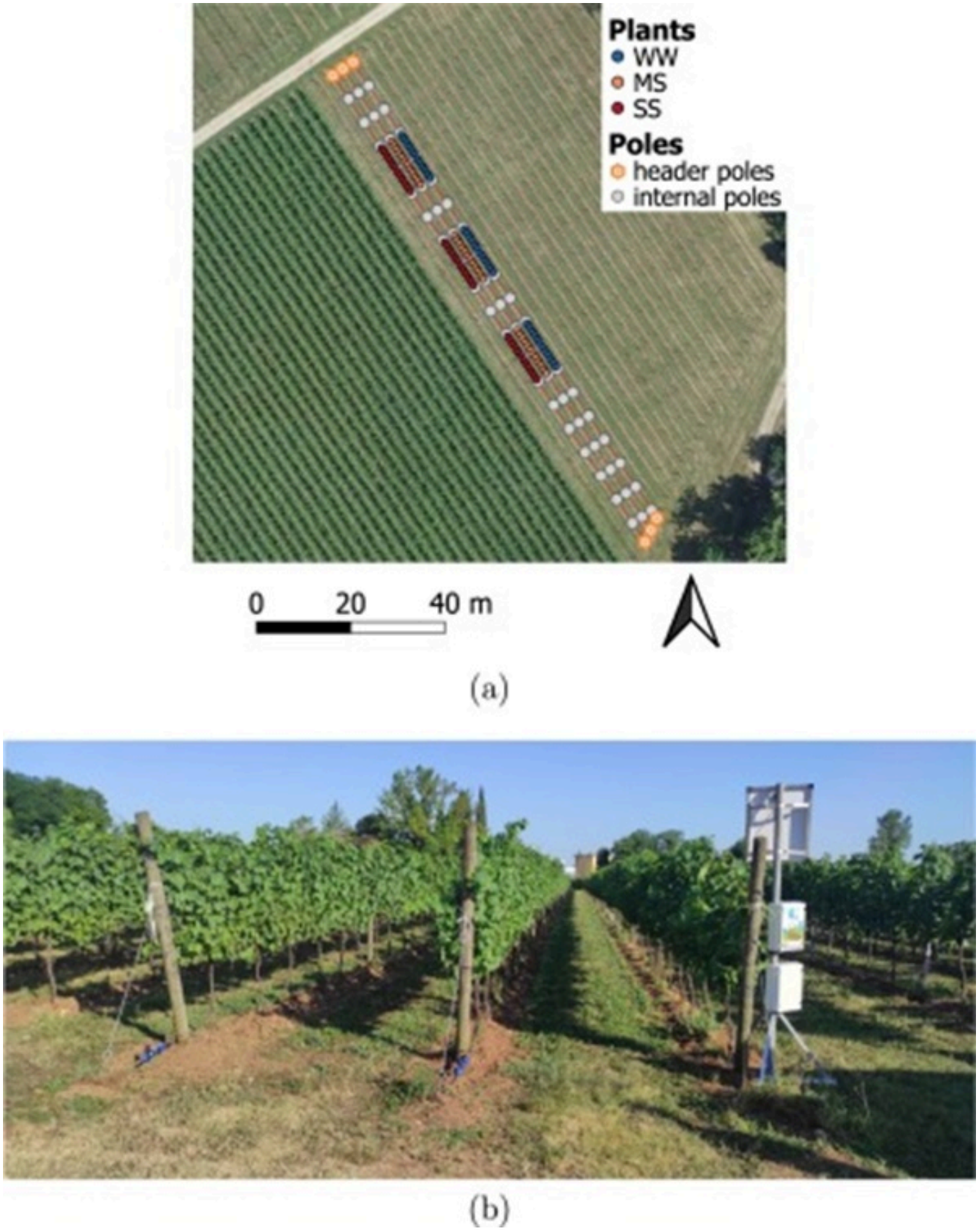

Figure 1. Vineyard site: (a) the location of plants, header, and internal poles in a top view of the vineyard (true orthophotography RAFVG 2017-2020, provided by IRDAT under IODL 2.0 license, was used as background layer); (b) entrance of the vineyard rows showing the irrigation control unit and part of the sub-irrigation system.

© 2025 The Author(s). | Published by Agro Intelligence Research Press

Three neighboring rows within the vineyard formed the study zone, spanning nearly 117×10 m² **(Figure 2)**. In every row, three plots each containing 12 similar plants were picked, according to the layout in **Figure 1**. Up to flowering, vines in every treatment group received complete irrigation. Afterward, each row received its own water regime, calibrated to maintain mean pre-dawn water potential (Ψpd) within defined ranges. Because Ψpd functions as a solid indicator of soil water potential, this setup supported the evaluation of three distinct water treatments (from flowering to harvest):

• Well watered (WW), Ψpd=−0.2 MPa

• Moderate stress (MS), Ψpd=−0.35 MPa

• Severe stress (SS), Ψpd=−0.55 MPa



Figure 2. Inspected vineyard rows: (a) well-watered row, (b) medium stressed row, and (c) severely stressed row.

The broad set of experiments outlined here relied on three instruments: a Scholander chamber to measure water potential, a UAV to capture multispectral images, and a mobile robot to build 3D plant models. Collected information was examined to obtain water potential values, vegetation indices, and geometric data, following the process shown in **Figure 3**. Outputs from the mobile robot and UAV were strongly linked, allowing spectral details to be extracted from precise target zones and plant spatial differences to be studied. In practice, UAV multispectral images were segmented using point clouds from the mobile robot, enabling vegetation index calculations exclusively on genuine plant surfaces while bypassing areas outside the canopy. In addition, contrary to earlier research [43, 44], the mobile robot performed 3D canopy modeling to minimize occlusions and flawed volume assessments caused by shifts in canopy thickness between the upper and lower sections.

© 2025 The Author(s). | Published by Agro Intelligence Research Press

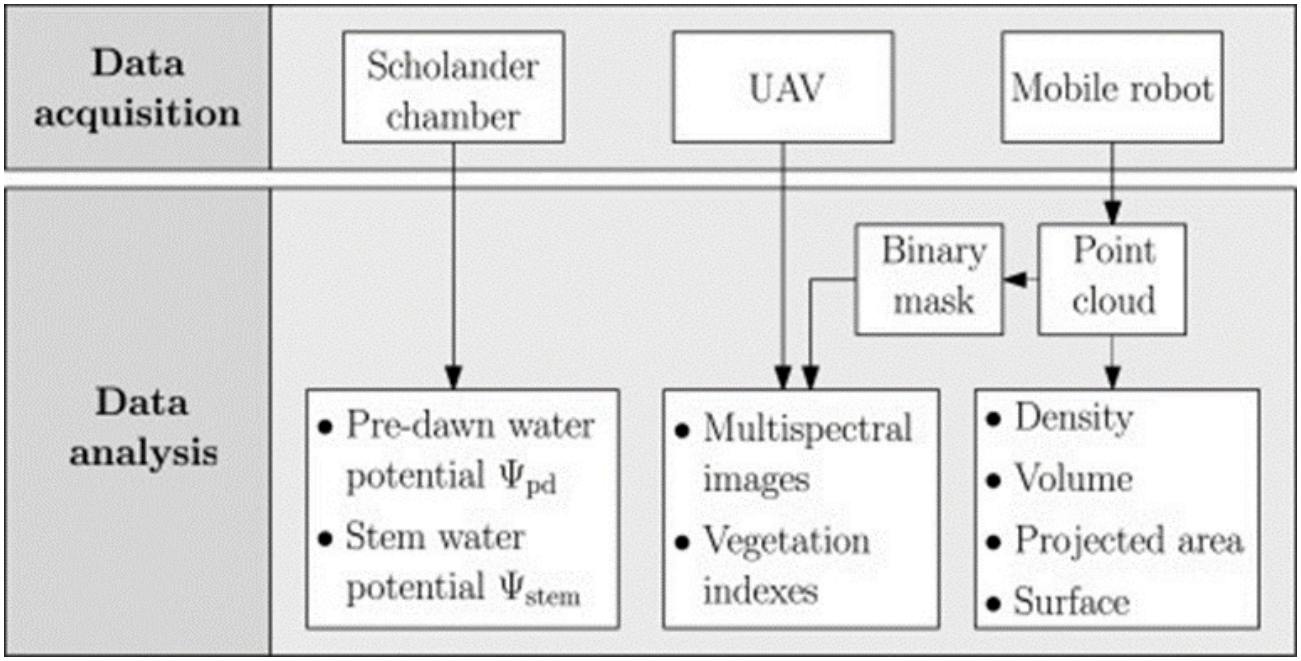

Figure 3. Description of the data acquisition and analysis.

Physiological measurements

Monitoring of plant water condition involved recording stem water potential (Ψstem) and pre-dawn water potential (Ψpd). Every water potential assessment was conducted on 28/07/2022 (62 days after full bloom, DAFB) using a Scholander chamber (Soil Moisture Corp., USA), in accordance with the guidelines of Scholander *et al.* [57]. Both Ψstem and Ψpd determinations used nine samples per water regime (n = 27), drawn from three separate leaves of distinct plants across each of the three plots.

Acquisition of multispectral indexes using a UAV

Collection of aerial information occurred through one midday flight on 28/07/2022 (62 DAFB) during suitable weather, with a DJI P4 multispectral UAV (SZ DJI Technology Co., Ltd., Beijing, China) that included an RTK-GNSS module by the same producer **(Figure 4)**. This small UAV carried six cameras total — one RGB and five covering separate spectral ranges: blue (450 nm ± 16 nm), green (560 nm ± 16 nm), red (650 nm ± 16 nm), red-edge (730 nm ± 16 nm), near-infrared (840 nm ± 26 nm). Flight height reached 20 m above ground and covered roughly 0.48 ha. In total, 2220 images were captured by the UAV and later processed in PIX4Dmapper (version 4.8.0; Pix4D, Switzerland) to create multispectral and RGB georeferenced rasters. Additional processing steps used the EPSG 6708 system (RDN2008 / UTM zone 33N (N-E)).

© 2025 The Author(s). | Published by Agro Intelligence Research Press



Figure 4. (a) The DJI P4 multispectral UAV, and (b) the multispectral and RGB cameras.

Linking physiological readings to multispectral outputs involved computing sixty vegetation indices (achievable from the captured spectral bands) referenced in Giovos *et al.* [58] across the five bands. An expanded collection of VIs — exceeding those typically used for stress detection — was considered. All VIs were computed using raster-based operations in the terra and raster packages of the R Statistical language (version 4.2.2; R Core Team, Austria).

Correlation checks compared average plot stem water potential figures against the vegetation indexes. Selection of nine representative indexes from the sixty relied on the strongest R^2 combined with the smallest p-value. The chosen nine VIs align with four out of five usage categories noted in Giovos *et al.* [58], which are distinguished by their spectral band pairings. **Table 1** lists the selected VIs, the involved bands, the calculation formulas, and the usage categories. The biomass and vegetation density category, driven mostly by NIR-red band pairings, appeared most frequently.

Table 1. Description of the nine selected VIs: equations and usage category [58].

Water potential	VI	Equation	Usage category
Ψ_{pd}/Ψ_{stem}	GDVI	$\mathrm{NIR} - \mathrm{G}$	Biophysical parameters
Ψ_{pd}/Ψ_{stem}	PVI	$\sqrt{(0.335\mathrm{NIR} - 0.149\mathrm{R})^2 + (0.335\mathrm{R} - 0.149\mathrm{NIR})^2}$	Biomass/vegetation density
Ψ_{pd}/Ψ_{stem}	TGI	$\mathrm{G} - 0.39\mathrm{R} - 0.61\mathrm{B}$	Pigments
Ψ_{stem}	2GRBi	$2\mathrm{G} - (\mathrm{R} + \mathrm{B})$	Pigments
Ψ_{stem}	DVI	$\mathrm{NIR} - \mathrm{R}$	Biomass/vegetation density
Ψ_{stem}	EVI2	$2.5\,(\mathrm{NIR} - \mathrm{R}) / (\mathrm{NIR} + 2.4\mathrm{R} + 1)$	Biomass/vegetation density

© 2025 The Author(s). | Published by Agro Intelligence Research Press

Ψ_{stem}	MCARI1	$1.2\,(2.5\,(\mathrm{NIR} - \mathrm{R}) - 1.3\,(\mathrm{NIR} - \mathrm{G}))$	Chlorophyll
Ψ_{stem}	MRVI	$(\mathrm{R} - 1)\,/\,(\mathrm{NIR} - 1)$	Biomass/vegetation density
Ψ_{stem}	MTVI1	$1.2\,(1.2\,(\mathrm{NIR} - \mathrm{G}) - 2.5\,(\mathrm{R} - \mathrm{G}))$	Biophysical parameters

Acquisition of the canopy status using a mobile robot

Point cloud collection for the vineyard occurred on 26/07/2022 (60 DAFB) with the Scout 2.0 mobile robotic platform (AgileX Robotics, Shenzen, China) pictured in **Figure 5**. Equipped with four electric motors, the robot included a Jetson Xavier onboard computer (NVIDIA, Santa Clara, USA) featuring an Octal-core NVIDIA Carmel ARMv8.2 CPU @ 2.26GHz, 512-core Volta GPU with 64 Tensor Cores, and 32GB 256-bit LPDDR4x @ 2133MHz memory. It also carried a RealSense D435 camera (Intel, Santa Clara, USA) and a 16-channel VLP-16 LiDAR sensor (Velodyne, Santa Clara, USA). This LiDAR unit provided a range of up to 100 m, ±3 cm accuracy, a 360° horizontal field of view, and a 30° vertical field of view (± 15°). **Figure 5b** displays the LiDAR coordinate setup.



Figure 5. (a) The Scout 2.0 mobile robot, and (b) close view of the robot electronics and LiDAR sensor.

Data gathering involved teleoperated travel along four vineyard paths, each about 117 m in length, with a return to the initial position. Such movement enabled side-by-side scanning of all plants in the three target rows.

Recorded LiDAR information using ROS Melodic on Ubuntu 18.04 and stored the data in ROS Bags format. Reconstruction of the 3D setting through SLAM required replaying the ROS Bags files at recorded speed on a workstation (Intel Core i5-10600K CPU @ 4.1GHz × 12; 32 GB RAM; 64-bit OS) also running Ubuntu 18.04 and ROS Melodic. Vineyard 3D modeling employed the graph-based Real-Time Appearance-Based Mapping (RTAB-Map) SLAM algorithm [59], which relies on Iterative Closest Point (ICP) with point-to-plane matching and loop closure refinement.

After SLAM processing, the complete 3D point cloud was refined in the open-source CloudCompare software, allowing isolation of each examined row. **Figure 6** summarizes the steps for handling point clouds. Application of the Statistical Outlier Removal (SOR) filter [60] cleared outliers and motion-induced noise, using 20 neighboring points and a standard

© 2025 The Author(s). | Published by Agro Intelligence Research Press

deviation multiplier of 1.00. The Cloth Simulation Filter (CSF) [61] then separated ground and vegetation points at a 0.5 m cloth resolution, with up to 1000 iterations and a 0.5 classification threshold. SOR filtering was performed first because RTAB-Map clouds show significant noise near the ground, and preliminary cleaning improves CSF effectiveness.

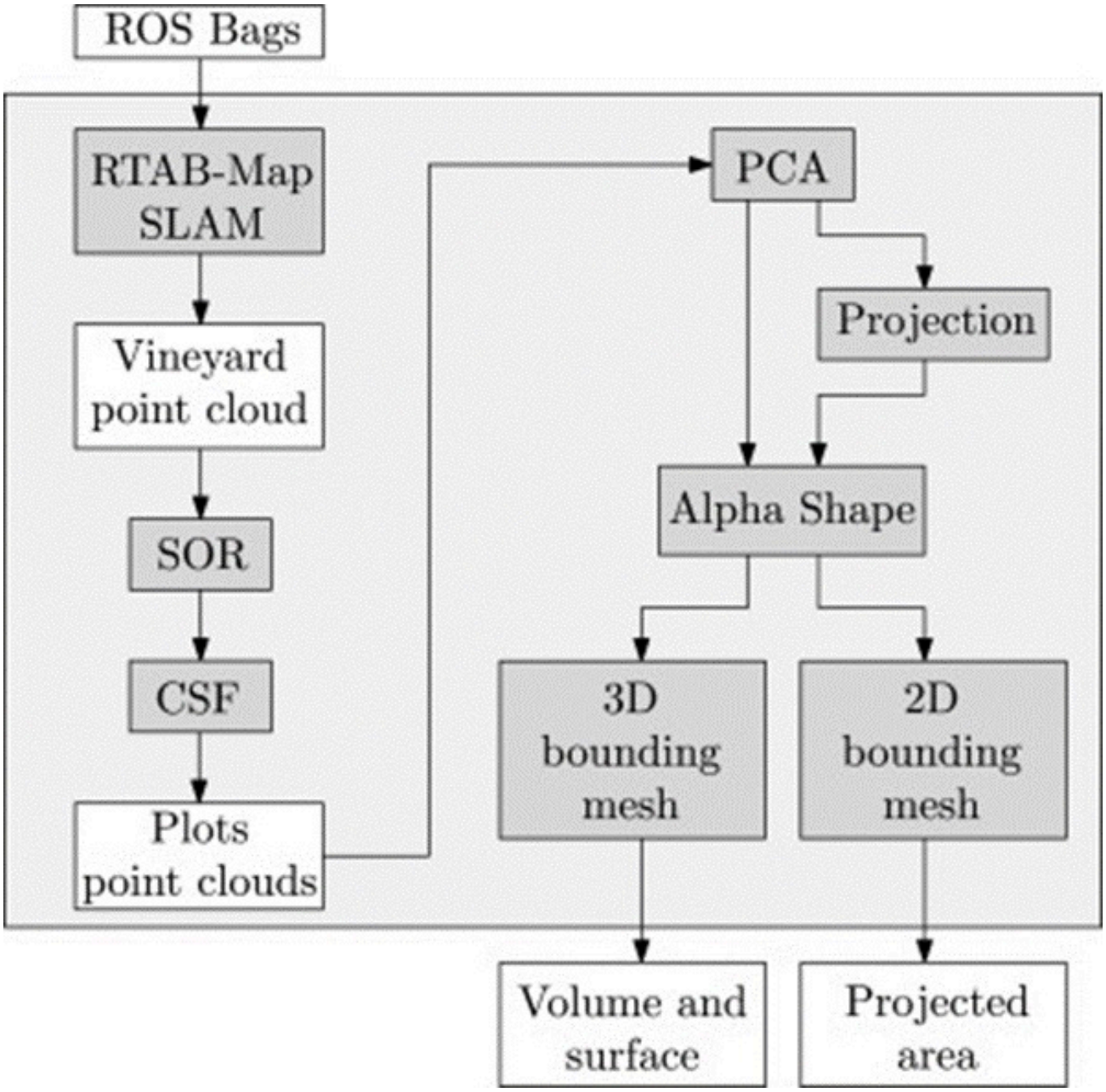

Figure 6. Overview of the point cloud processing.

Two binary masks (images showing 0 where no vegetation exists and 1 where vegetation is present) were created in QGIS (version 3.22.11-Białowieża; QGIS.ORG, Switzerland) after projecting the cleaned point cloud downward onto the ground plane along the vertical direction. Regarding an image I, the pixels {p(i,j)} that cover the vineyard plots constitute a subset $V \subset I$, satisfying $(i,j) \in V$ only when the pixel p(i,j) falls within the plots. Generation of the binary mask follows this process:

© 2025 The Author(s). | Published by Agro Intelligence Research Press

$$p(i,j) = \begin{cases} 1, & \text{if } (i,j) \in V \\ 0, & \text{otherwise} \end{cases} \quad (1)$$

The initial binary mask was derived from points at trunk level, and the second mask was derived from the full point cloud. This trunk-level mask enabled georeferencing the second mask to EPSG 6708 using the raster georeferencer tool in QGIS. Header poles **(Figure 1)** served visibly as control points. Following this, vineyard plot segmentation applied the second binary mask.

Each row yielded three plots isolated from point cloud segments through distance calculations from the vineyard header pole—cloudCompare calculated point density for each point using neighbors within a 0.1 m radius. Retrieval of plant volume and surface estimates used the Alpha Shape algorithm [62] available in Matlab® (version R2022b; The MathWorks Inc.®, Natick, MA, USA). Matlab® automatically determined the critical radius for each point cloud — the smallest value that, when triangulated (meshed), yields a bounding area or volume that fully encloses all points. Triangles from the mesh that touch the vineyard plot section planes were excluded during surface computation, since they fail to capture the actual plot geometry.

Further canopy size examination in the selected vineyard rows involved computing the area of plants projected onto the ground. The projection axis came from Principal Component Analysis (PCA). With the three primary directions identified, projection along the vertical axis produced a 2D point collection. The Alpha Shape algorithm was applied to each 2D collection, yielding the projected area for each. **Algorithm 1** outlines the Matlab® procedure developed for obtaining size metrics.

1: **Input:** Point cloud data
2: **Output:** Bounding mesh *volume*, *surface*, and *projected area*
3: Import point cloud
4: Perform PCA analysis to define the principal axis
5: Compute α^* for the 3D bounding mesh
6: Compute the 3D bounding mesh using the Alpha Shape algorithm
7: Compute *volume* and *surface* of the 3D bounding mesh
8: Project the point cloud along the vertical axis
9: Compute α^* for the 2D bounding mesh
10: Compute the 2D bounding mesh using the Alpha Shape algorithm
11: Compute the *projected area* of the 2D bounding mesh

Algorithm 1. Analysis of the point cloud.

Statistical analysis

Evaluation of results included statistical processing. Links among numerical factors — physiological data, multispectral indices, and geometric quantities — were tested using one-way ANOVA. Significant outcomes led to mean separation by post-hoc Tukey test (p-value<0.05). Checks for residual normality and variance equality used Shapiro-Wilk and Levene's tests. Spearman correlations additionally examined relationships between variables.

Results and Discussion

© 2025 The Author(s). | Published by Agro Intelligence Research Press

A sample vineyard row section appears reconstructed in 3D in **Figure 7**, where color variations mark differing point density. Density clearly varies between upper and lower canopy sections. **Figure 8** demonstrates the creation of a 3D bounding mesh for one experimental plot, alongside its 2D projected area mesh, both derived from mobile robot point clouds. Black dashed lines denote the main axis through the 3D point cloud. **Figure 9** further displays segmentation outcomes, including a top view of experimental plot masks over NIR background plus enlarged plot details.

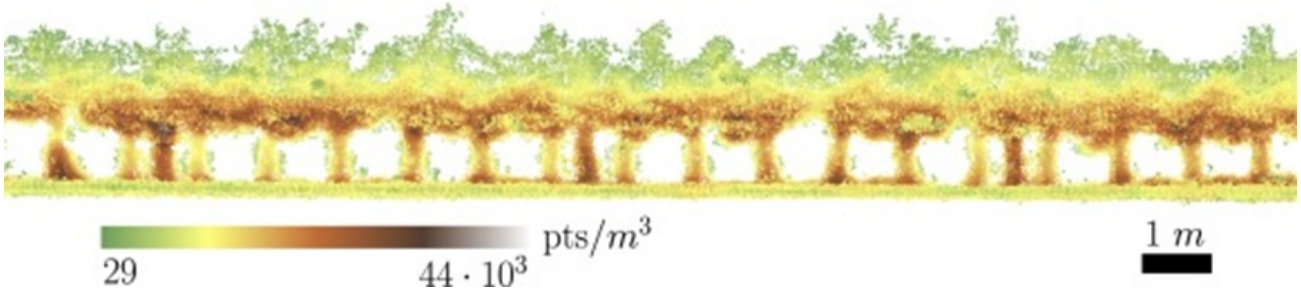

Figure 7. 3D reconstruction of an example portion of a vineyard row (side view). The colors represent different values of point density.

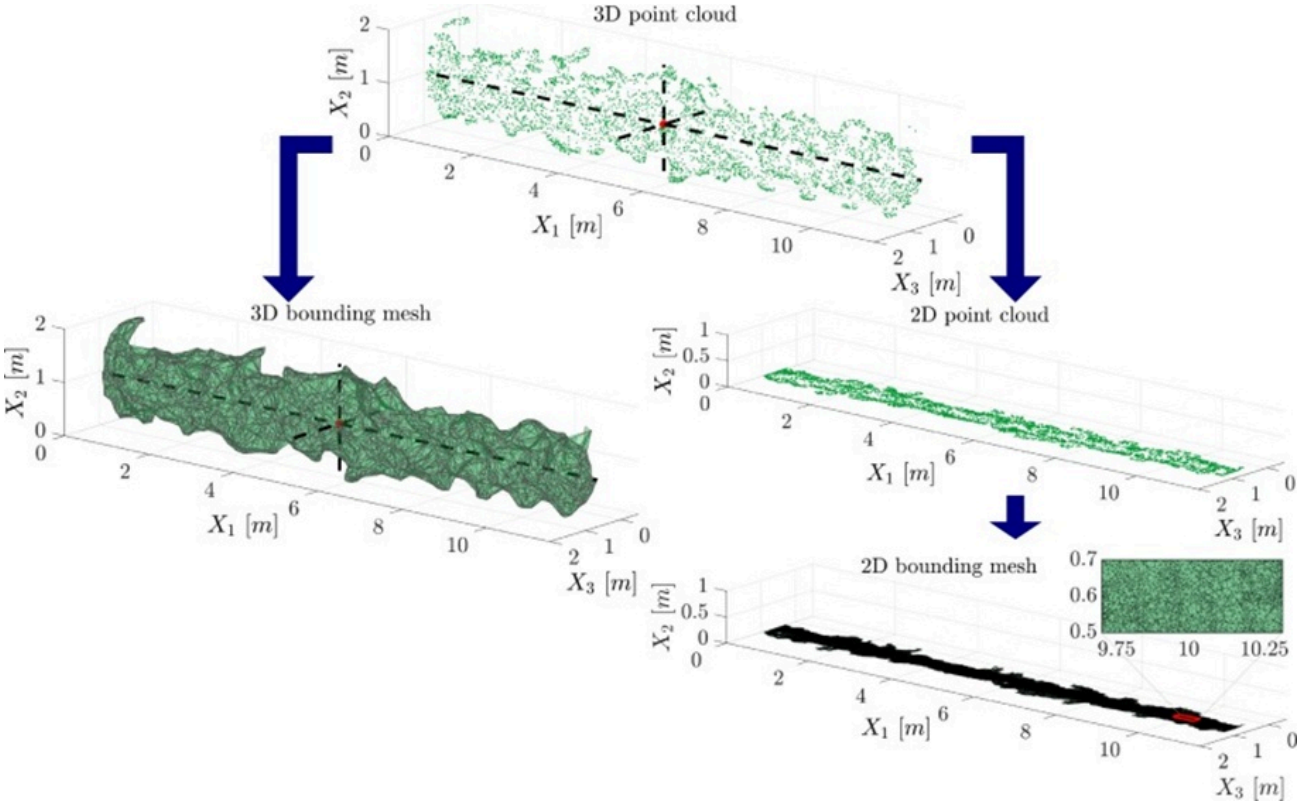

Figure 8. Example of the reconstruction of the 3D bounding mesh of a vineyard experimental plot (left) and of the 2D bounding mesh of the projected area (right), starting from the 3D point cloud acquired by the mobile robot. The black dashed axis represents the principal axis of the 3D point cloud.

© 2025 The Author(s). | Published by Agro Intelligence Research Press

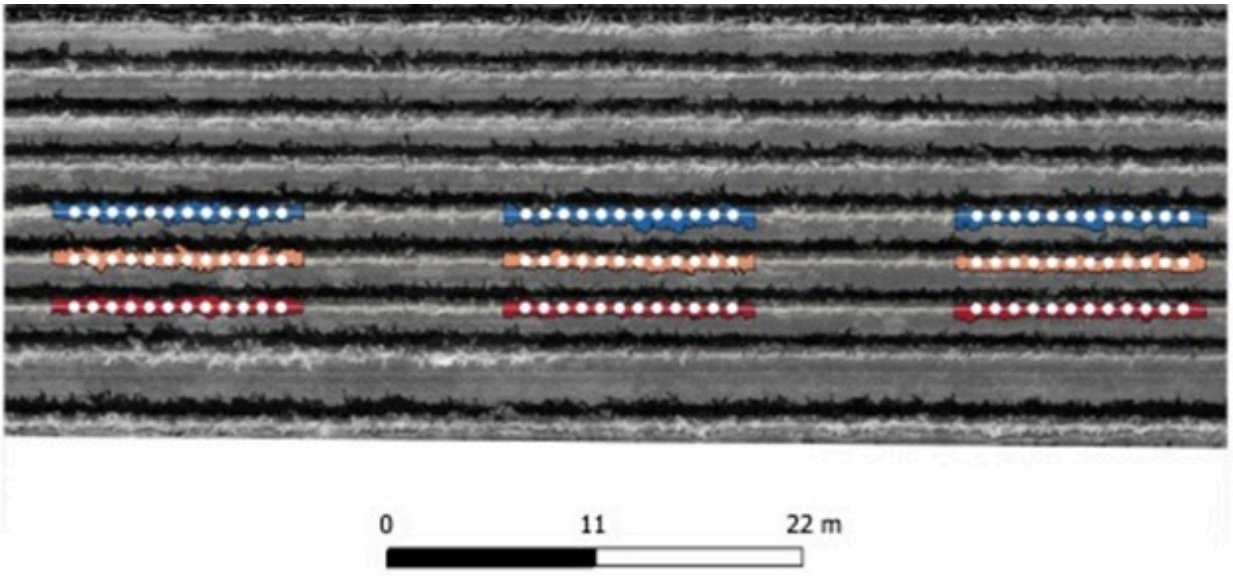

(a)

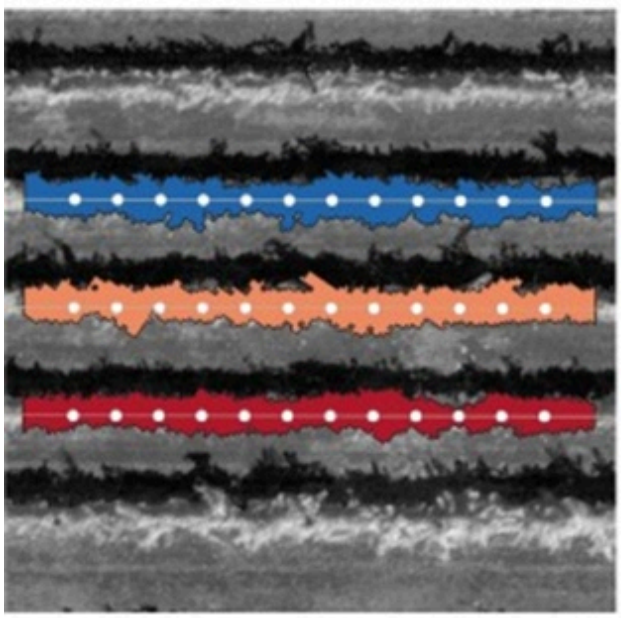

(b)

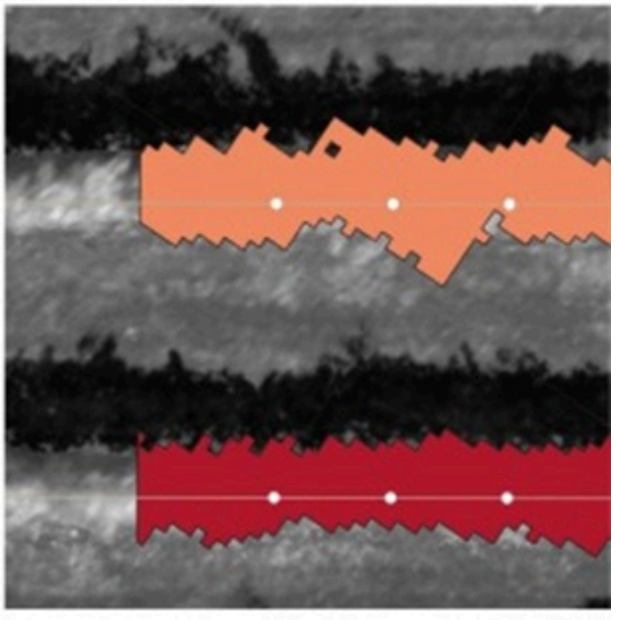

(c)



© 2025 The Author(s). | Published by Agro Intelligence Research Press



Table 2 summarizes one-way ANOVA findings for physiological and geometric variables, listing means, standard deviations, and Tukey test outcomes. Significance appears in the table's last column. Tests verified normal residuals and equal variances (results not shown).

Table 2. Results of the one-way ANOVA analysis performed on physiological and geometrical parameters. If the ANOVA test yields significant results, the mean values are separated using the post hoc Tukey test. n.s.: not significative; ∗: P-value < 0.05; ∗∗: P-value < 0.01.

Parameter	Unit	Result	Water regime		
			SS	MS	WW
Ψ_{stem}	MPa	∗∗	−0.98 ± 0.09	−0.75 ± 0.10	−0.57 ± 0.10
Ψ_{pd}	MPa	∗∗	−0.18 ± 0.02	−0.16 ± 0.01	−0.12 ± 0.01
Canopy volume	m^3	n.s.	4.80 ± 0.89	5.60 ± 0.18	6.37 ± 0.92
Surface	m^2	n.s.	50.95 ± 3.26	48.85 ± 6.84	50.07 ± 0.30
Projected area	m^2	∗	6.99 ± 0.42	7.83 ± 0.52	8.70 ± 0.33
Points density	pts/m^3	n.s.	21539 ± 889	20674 ± 536	20616 ± 1352

Initial assessment focused on Scholander chamber data. Box plots in **Figure 10** visualize treatment differences (WW, MS, SS) per row. WW and SS treatments differed as predicted, while MS occupied an intermediate position (Ψstem: p-value=0.00775, Ψpd: P-value=0.00697) in both stem **(Figure 10a)** and pre-dawn **(Figure 10b)** potentials. Water potential rose consistently with increasing water supply. Matching patterns for Ψpd and Ψstem allowed clear separation of the three regimes across rows.

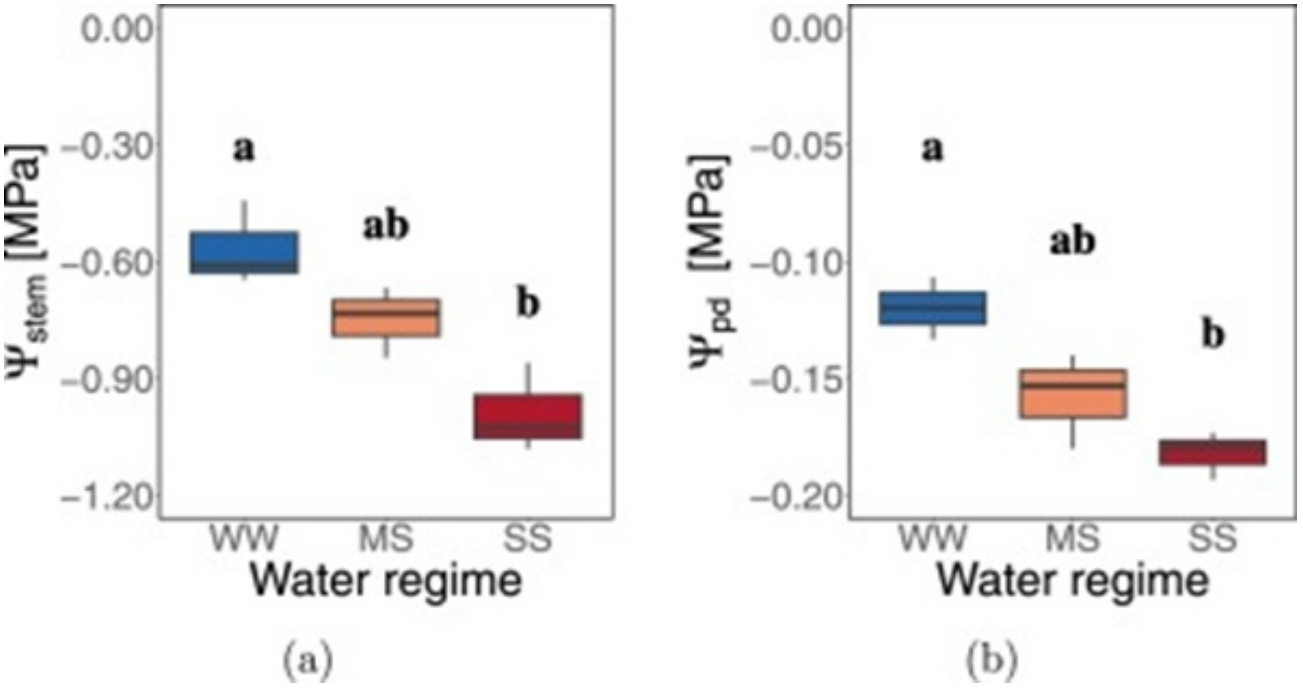

© 2025 The Author(s). | Published by Agro Intelligence Research Press

Figure 10. Results of water potential measured with the Scholander chamber: (a) stem water potential; (b) pre-dawn water potential. In case of significant results of the one-way ANOVA test, mean values are separated using the post-hoc Tukey test. Different letters indicate statistically significant differences. Variables with no common letters are significantly different.

Correlations between stem water potential and the nine selected VIs are shown in **Figure 11**, with regression lines and 95% confidence intervals (grey zones). Significant group differences emerged from the VI P-values. Strong positive correlations linked all nine VIs to stem water potential (GDVI: R2 = 0.90, PVI: R2 = 0.90, TGI: R2 = 0.87, 2GRBi: R2 = 0.84, DVI: R2 = 0.78, EVI2: R2 = 0.78, MCARI1: R2 = 0.78, MRVI: R2 = 0.78, MTVI1: R2 = 0.78).

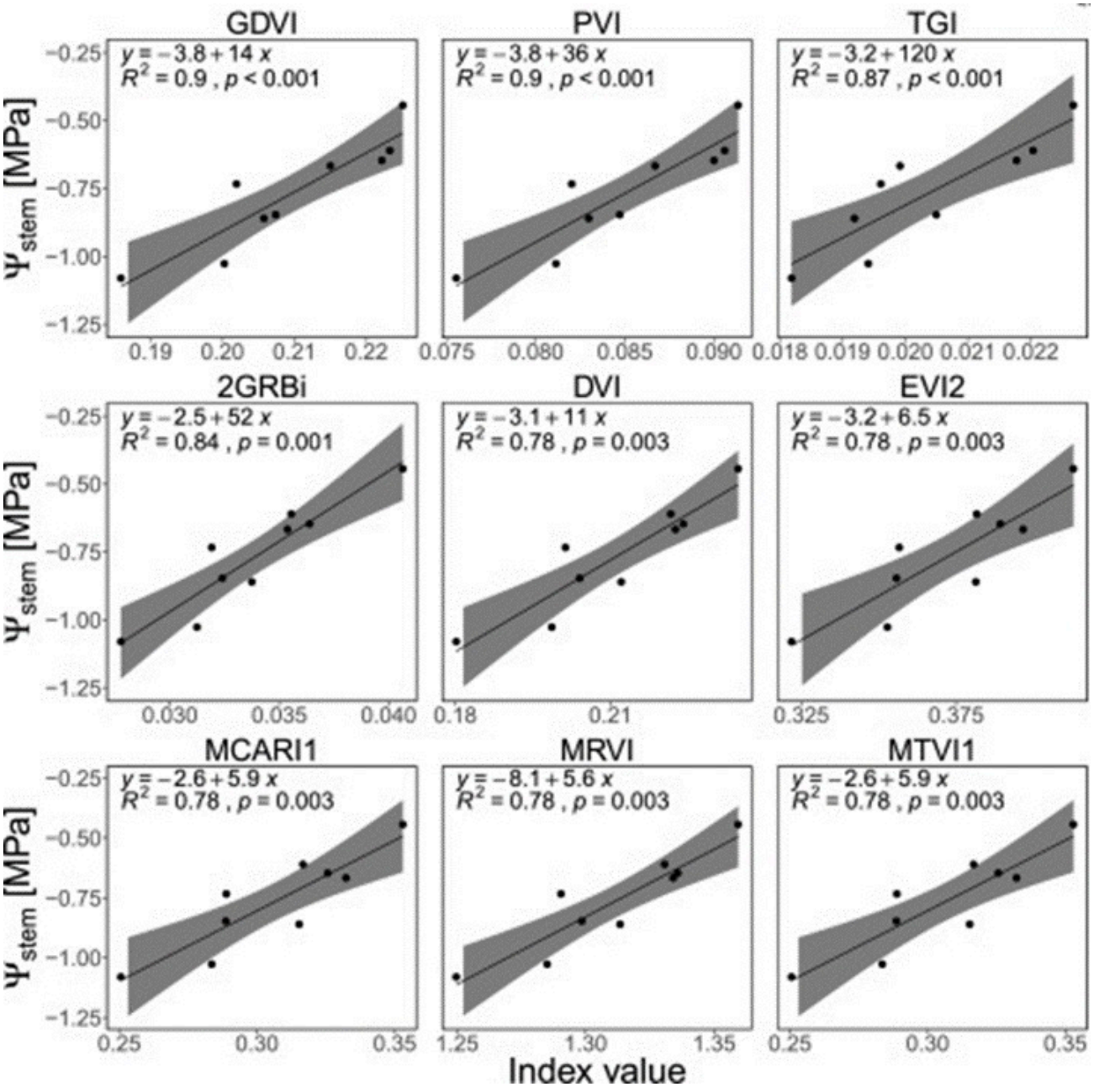

Figure 11. Results of the correlation analysis between the stem water potential and the vegetation indices. Points indicate the mean plot stem water potential values, correlated with the mean plot VI values. The black line represents the

© 2025 The Author(s). | Published by Agro Intelligence Research Press

regression line, and the grey area indicates the confidence interval (95%). The regression line equation, R2, and the Spearman correlation coefficient are reported for each plot on the top-left side.

Pre-dawn water potential correlations with VIs followed the same approach. **Figure 12** shows regression lines and 95% confidence intervals for Ψpd. Only three VIs surpassed R2 = 0.5: TGI (R2 = 0.77), GDVI (R2 = 0.57), and PVI (R2 = 0.57). Positive relationships appeared with pre-dawn water potential. Alignment with soil moisture reinforced validation of the three field water regimes.

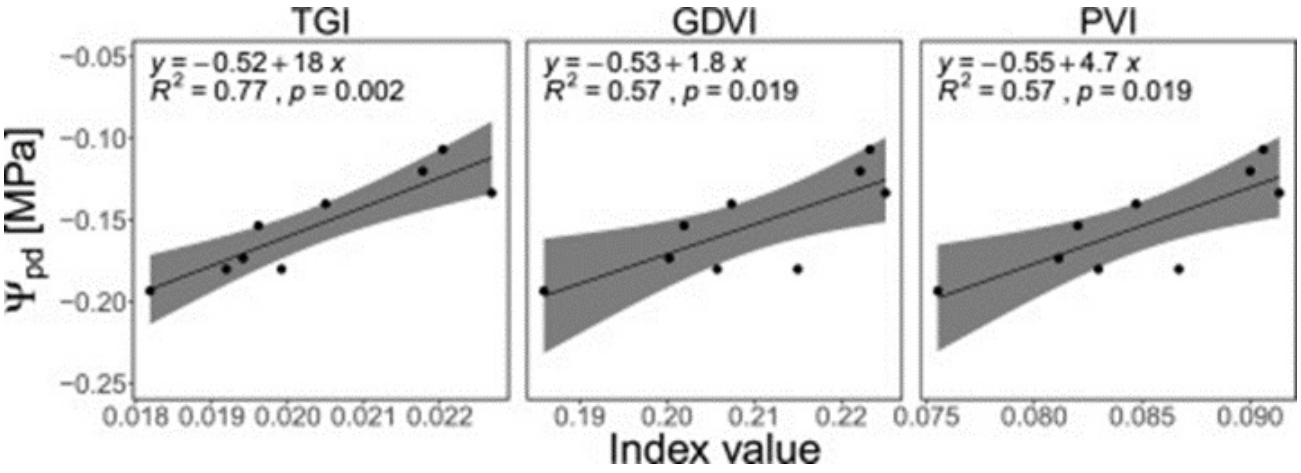

Figure 12. Results of the correlation analysis between the pre-dawn water potential and the vegetation indices. Points indicate the pre-dawn water potential and the VIs of the plot, which are correlated with the plot's mean pre-dawn water potential. The black line represents the regression line, and the grey area indicates the confidence interval (95%). The regression line equation, R2, and the Spearman correlation coefficient are reported for each plot on the top-left side.

Figure 13 box plots display geometric parameters by water regime. Canopy volume, bounding surface, and projected area **(Figure 13a-13c)** increased alongside water availability. WW projected area differed statistically from SS according to **Table 2**. Volume, point density, and surface showed no significant differences across regimes, yet clear trends emerged. Volume rose 13.75% in WW versus MS, dropped 14.29% in SS versus MS, and increased 32.71% in WW versus SS.

© 2025 The Author(s). | Published by Agro Intelligence Research Press

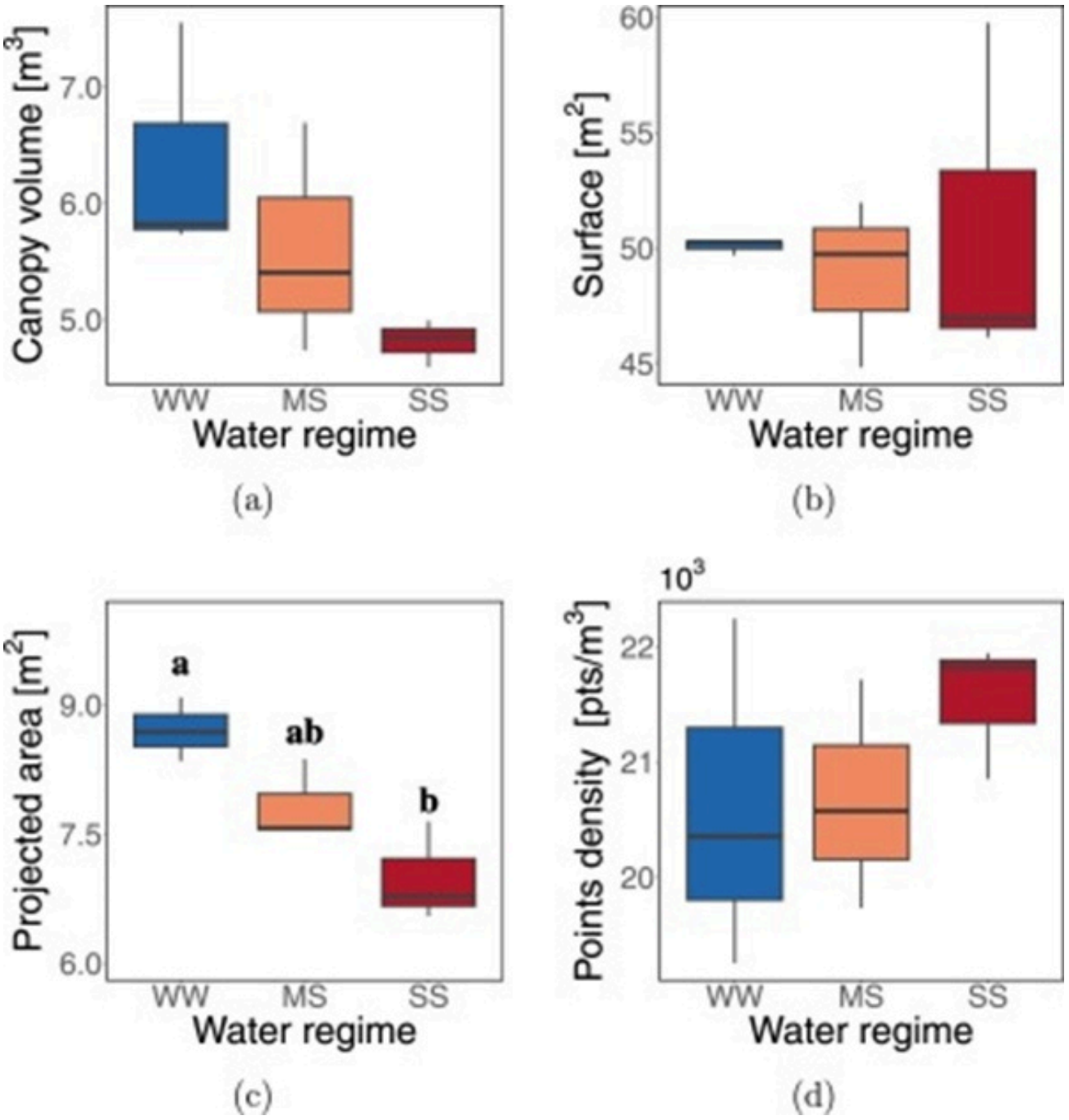

Figure 13. Results of the 3D reconstruction of the canopy: (a) volume; (b) bounding surface; (c) projected area; and (d) point density. In case of significant results of the one-way ANOVA test, mean values are separated using the post-hoc Tukey test. Different letters indicate statistically significant differences. Variables with no common letters are significantly different.

Regression analysis connected geometric data to Scholander measurements. Strong links formed between stem water potential and both canopy volume and projected area. **Figure 14** illustrates these regressions with lines and 95% confidence intervals. Positive correlations emerged for both geometric factors with stem water potential. Significant p-values were observed, yielding R2 = 0.72 for volume and R2 = 0.67 for projected area.

© 2025 The Author(s). | Published by Agro Intelligence Research Press

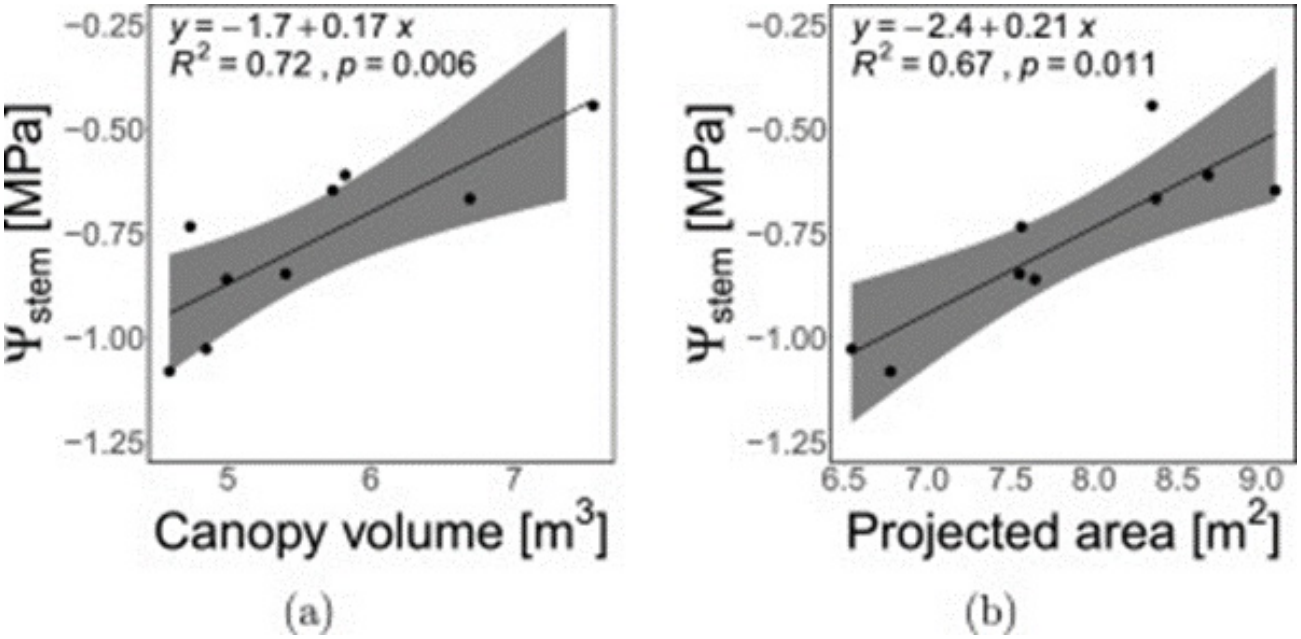

Figure 14. Results of the correlation analysis between the stem water potential and the geometrical measurements: (a) canopy volume; (b) projected area. Points indicate the mean plot stem water potential, correlated with the mean canopy volume and projected plot area. The black line represents the regression line, and the grey area indicates the confidence interval (95%). The regression line equation, R2, and the Spearman correlation coefficient are reported for each plot on the top-left side.

Discussion

Merging UAV and mobile robot data successfully captured spatial differences in the grapevine canopy using a mask. Masks restricted UAV spectral extraction to canopy zones alone, limiting contamination from soil or inter-row vegetation. High R2 values confirmed strong relationships between the extracted indexes and physiological indicators. Expanding the range of vegetation indices also deepened insight into the true state of plants. Both water potential types yielded favorable results, informing future VI deployment for direct plant stress evaluation (stem water potential) and soil moisture estimation (pre-dawn water potential).

Mobile robot measurements of canopy volume and projected area supported the impact of distinct water regimes on growth patterns. A ground robot and UAV combination for 3D canopy modeling offered clear benefits for detailed internal inspection, sub-volume assessment, and occlusion reduction in areas where density varies vertically.

Volume and projected area outcomes aligned with agronomic principles: water limitation restricts above-ground expansion [7, 63], producing smaller dimensions in stressed plants than in well-watered ones. These differences do not arise directly from water content itself. Water-content VIs normally require NIR-SWIR band pairs [58], unavailable on the DJI P4 UAV or comparable platforms. Present indexes instead leaned geometric **(Table 1, last column)** and aligned closely with standard biomass and density indicators.

Controlled regimes began at bloom, providing adequate time for differential growth. **Figure 13** highlights how water volume shapes canopy volume and surface area. Uncontrolled or brief stress periods might limit the use of geometric metrics as water-status proxies. Combining biomass VIs with physiological activity VIs would then prove helpful by incorporating chlorophyll, pigment, and biophysical categories **(Table 1)**. Best VIs here also differed from common choices for mobile robots, such as NDVI or NDRE [23, 41].

© 2025 The Author(s). | Published by Agro Intelligence Research Press

This strategy fits controlled regimes influencing development and canopy scale **(Figures 13 and 14)**. Temporary stress detection would require other methods, such as thermal sensing [64].

Upcoming work will gather full-season measurements, as in Polvara *et al.* [65], to map extended connections among water regime, indices, and geometry. Extension to short-term stress will involve adding a multispectral camera to the robot. Full automation of navigation and processing will reduce manual input. Deep learning models [66, 67] will support direct stress detection from drone and robot images.

Conclusion

This study introduces an innovative technique to assess how water regimes affect grapevine canopy conditions, using robotics for observation and mapping. Multispectral images and various vegetation indices were collected by an unmanned aerial vehicle (UAV), while the ground mobile robot provided the 3D canopy reconstruction. In contrast to earlier studies, 60 vegetation indices were calculated exactly using the vineyard point cloud's projected area as a mask. Detailed field trials on replicated Pinot gris vine plots revealed that the GDVI, PVI, and TGI vegetation indexes maintain positive correlations with water potential: GDVI (R2 = 0.90 and 0.57 for the stem and pre-dawn water potential, respectively), PVI (R2 = 0.90 and 0.57), TGI (R2 = 0.87 and 0.77). Moreover, both canopy volume and ground-projected canopy area respond to water status, along with stem and pre-dawn water potential readings. Findings from this research confirm the viability of the suggested technique and illustrate the value of robotic systems for advancing precision viticulture.

Acknowledgements

The authors would like to thank Dr. Eleonora Maset for her suggestions on point cloud processing and Mr. Michele Mestroni for providing the UAV used in this work.

Conflict of interest

None

Financial support

This study was carried out within the Agritech National Research Center and received funding from the European Union Next-Generation EU (Piano Nazionale di Ripresa e Resilienza (PNRR) – Missione 4 Componente 2, Investimento 1.4 - D.D. 1032 17/06/2022, CN00000022). This manuscript reflects only the authors' views and opinions; neither the European Union nor the European Commission can be considered responsible for them.

This research was partially developed within the Laboratory for Big Data, IoT, Cyber Security (LABIC), funded by the Friuli Venezia Giulia Region, and the Laboratory for Artificial Intelligence for Human-Robot Collaboration (AI4HRC), funded by Fondazione Friuli.

The first author acknowledges support from the National Ph.D. Programme in Artificial Intelligence of the University of Naples Federico II (Naples, Italy).

Ethics statement

None

© 2025 The Author(s). | Published by Agro Intelligence Research Press

Received: 06 Nov 2023 Revised: 11 Jan 2024 Accepted: 26 Jan 2024
Published online: 25 May 2025

Rights and permissions

Open Access The author(s) retain copyright. This article is licensed under the Creative Commons Attribution-NonCommercial-ShareAlike 4.0 International License. It may be shared and adapted for non-commercial purposes with appropriate attribution, an indication of changes, and distribution of adaptations under the same license. Third-party material may be subject to separate terms identified in its credit line. View the license at https://creativecommons.org/licenses/by-nc-sa/4.0/.

References

1. Lesk C, Rowhani P, Ramankutty N. Influence of extreme weather disasters on global crop production. Nature. 2016;529:84-7.
2. Arias PA, Bellouin N, Coppola E, Jones R, Krinner G, Marotzke J, et al. Climate change 2021: The physical science basis. Contribution of Working Group I to the Sixth Assessment Report of the Intergovernmental Panel on Climate Change, Technical Summary. IPCC Intergovernmental Panel on Climate Change; 2021.
3. Van Leeuwen C, Darriet P. The impact of climate change on viticulture and wine quality. J Wine Econ. 2016;11:150-67.
4. Lei Y, Zhang H, Chen F, Zhang L. How rural land use management facilitates drought risk adaptation in a changing climate: A case study in arid northern China. Sci Total Environ. 2016;550:192-9.
5. Bandurska H. Drought stress responses: Coping strategy and resistance. Plants. 2022;11:922.
6. Brodribb T, Brodersen CR, Carriqui M, Tonet V, Rodriguez Dominguez C, McAdam S. Linking xylem network failure with leaf tissue death. New Phytol. 2021;232:68-79.
7. Toscano S, Scuderi D, Giuffrida F, Romano D. Responses of Mediterranean ornamental shrubs to drought stress and recovery. Sci Hortic. 2014;178:145-53.
8. Tankari M, Wang C, Ma H, Li X, Li L, Soothar RK, et al. Drought priming improved water status, photosynthesis and water productivity of cowpea during post-anthesis drought stress. Agric Water Manag. 2021;245:106565.
9. McDowell NG. Mechanisms linking drought, hydraulics, carbon metabolism, and vegetation mortality. Plant Physiol. 2011;155:1051-9.
10. Rienth M, Scholasch T. State-of-the-art of tools and methods to assess vine water status. Oeno One. 2019;53(4):619-37.
11. Garnier E, Berger A. Testing water potential in peach trees as an indicator of water stress. J Hortic Sci. 1985;60:47-56.
12. Martinez-Vilalta J, Poyatos R, Aguade D, Retana J, Mencuccini M. A new look at water transport regulation in plants. New Phytol. 2014;204:105-15.
13. Ihuoma SO, Madramootoo CA. Recent advances in crop water stress detection. Comput Electron Agric. 2017;141:267-75.
14. Gautam D, Pagay V. A review of current and potential applications of remote sensing to study the water status of horticultural crops. Agronomy. 2020;10:140.
15. Zhai Z, Martínez JF, Beltran V, Martínez NL. Decision support systems for agriculture 4.0: Survey and challenges. Comput Electron Agric. 2020;170:105256.

© 2025 The Author(s). | Published by Agro Intelligence Research Press

16. Matese A, Di Gennaro SF. Beyond the traditional NDVI index as a key factor to mainstream the use of UAV in precision viticulture. Sci Rep. 2021;11:1-13.

17. Tardaguila J, Stoll M, Gutiérrez S, Proffitt T, Diago MP. Smart applications and digital technologies in viticulture: A review. Smart Agric Technol. 2021;1:100005.

18. Wang K, Zhou J, Zhang W, Zhang B. Mobile LiDAR scanning system combined with canopy morphology extracting methods for tree crown parameters evaluation in orchards. Sensors. 2021;21:339.

19. Xue J, Su B. Significant remote sensing vegetation indices: A review of developments and applications. J Sens. 2017;2017.

20. Huang S, Tang L, Hupy JP, Wang Y, Shao G. A commentary review on the use of normalized difference vegetation index (NDVI) in the era of popular remote sensing. J For Res. 2021;32:1-6.

21. Bannari A, Morin D, Bonn F, Huete A. A review of vegetation indices. Remote Sens Rev. 1995;13:95-120.

22. Zine-El-Abidine M, Dutagaci H, Galopin G, Rousseau D. Assigning apples to individual trees in dense orchards using 3D colour point clouds. Biosyst Eng. 2021;209:30-52.

23. Pagliai A, Ammoniaci M, Sarri D, Lisci R, Perria R, Vieri M, et al. Comparison of aerial and ground 3D point clouds for canopy size assessment in precision viticulture. Remote Sens. 2022;14:1145.

24. Tiozzo Fasiolo D, Scalera L, Maset E, Gasparetto A. Towards autonomous mapping in agriculture: A review of supportive technologies for ground robotics. Robot Auton Syst. 2023;104514.

25. Manish R, Lin YC, Ravi R, Hasheminasab SM, Zhou T, Habib A. Development of a miniaturized mobile mapping system for in-row, under-canopy phenotyping. Remote Sens. 2021;13:276.

26. Rivera G, Porras R, Florencia R, Sánchez-Solís JP. LiDAR applications in precision agriculture for cultivating crops: A review of recent advances. Comput Electron Agric. 2023;207:107737.

27. Bietresato M, Carabin G, Vidoni R, Gasparetto A, Mazzetto F. Evaluation of a LiDAR-based 3D-stereoscopic vision system for crop-monitoring applications. Comput Electron Agric. 2016;124:1-13.

28. Vidoni R, Gallo R, Ristorto G, Carabin G, Mazzetto F, Scalera L, et al. ByeLab: An agricultural mobile robot prototype for proximal sensing and precision farming. ASME International Mechanical Engineering Congress and Exposition, American Society of Mechanical Engineers. 2017;V04AT05A057.

29. Siebers MH, Edwards EJ, Jimenez-Berni JA, Thomas MR, Salim M, Walker RR. Fast phenomics in vineyards: Development of GRover, the grapevine rover, and LiDAR for assessing grapevine traits in the field. Sensors. 2018;18:2924.

30. Escolà A, Martínez-Casasnovas JA, Rufat J, Arnó J, Arbonés A, Sebé F, et al. Mobile terrestrial laser scanner applications in precision fruticulture/horticulture and tools to extract information from canopy point clouds. Precis Agric. 2017;18:111-32.

31. Chakraborty M, Khot LR, Sankaran S, Jacoby PW. Evaluation of mobile 3D Light Detection and Ranging based canopy mapping system for tree fruit crops. Comput Electron Agric. 2019;158:284-93.

32. Wichmann M, Kamil M, Frederiksen A, Kotzur S, Scherl M. Long-term investigations of weather influence on direct time-of-flight lidar at 905 nm. IEEE Sens J. 2021;22:2024-36.

33. Jay S, Rabatel G, Hadoux X, Moura D, Gorretta N. In-field crop row phenotyping from 3D modeling performed using Structure from Motion. Comput Electron Agric. 2015;110:70-7.

© 2025 The Author(s). | Published by Agro Intelligence Research Press

34. Vulpi F, Marani R, Petitti A, Reina G, Milella A. An RGB-D multi-view perspective for autonomous agricultural robots. Comput Electron Agric. 2022;202:107419.

35. Tiozzo Fasiolo D, Scalera L, Maset E. Comparing LiDAR and IMU-based SLAM approaches for 3D robotic mapping. Robotica. 2023:1-17.

36. Cheein FAA, Guivant J. SLAM-based incremental Convex Hull processing approach for treetop volume estimation. Comput Electron Agric. 2014;102:19-30.

37. Cubero S, Marco-Noales E, Aleixos N, Barbé S, Blasco J. Robhortic: A field robot to detect pests and diseases in horticultural crops by proximal sensing. Agriculture. 2020;10:276.

38. Ulloa CC, Krus A, Barrientos A, del Cerro J, Valero C. Robotic fertilization in strip cropping using a CNN vegetables detection-characterization method. Comput Electron Agric. 2022;193:106684.

39. Fernández-Novales J, Saiz-Rubio V, Barrio I, Rovira-Más F, Cuenca-Cuenca A, Santos Alves F, et al. Monitoring and mapping vineyard water status using non-invasive technologies by a ground robot. Remote Sens. 2021;13:2830.

40. Saiz-Rubio V, Rovira-Más F, Cuenca-Cuenca A, Alves F. Robotics-based vineyard water potential monitoring at high resolution. Comput Electron Agric. 2021;187:106311.

41. Bietresato M, Carabin G, D'Auria D, Gallo R, Ristorto G, Mazzetto F, et al. A tracked mobile robotic lab for monitoring the plants volume and health. 2016 12th IEEE/ASME International Conference on Mechatronic and Embedded Systems and Applications (MESA), IEEE. 2016. p. 1-6.

42. Ristorto G, Gallo R, Gasparetto A, Scalera L, Vidoni R, Mazzetto F. A mobile laboratory for orchard health status monitoring in precision farming. Chem Eng Trans. 2017;58:661-6.

43. Martínez-Peña R, Vélez S, Vacas R, Martín H, Álvarez S. Remote sensing for sustainable pistachio cultivation and improved quality traits evaluation through thermal and non-thermal UAV vegetation indices. Appl Sci. 2023;13:7716.

44. Vélez S, Ariza-Sentís M, Valente J. Mapping the spatial variability of Botrytis bunch rot risk in vineyards using UAV multispectral imagery. Eur J Agron. 2023;142:126691.

45. Xie P, Du R, Ma Z, Cen H. Generating 3D multispectral point clouds of plants with fusion of snapshot spectral and RGB-D images. Plant Phenom. 2023;5:0040.

46. López A, Jurado JM, Ogayar CJ, Feito FR. An optimized approach for generating dense thermal point clouds from UAV-imagery. ISPRS J Photogramm Remote Sens. 2021;182:78-95.

47. Wang L, Miao Y, Han Y, Li H, Zhang M, Peng C. Extraction of 3D distribution of potato plant CWSI based on thermal infrared image and binocular stereovision system. Front Plant Sci. 2023;13:1104390.

48. Narváez FJY, del Pedregal JS, Prieto PA, Torres-Torriti M, Cheein FAA. LiDAR and thermal images fusion for ground-based 3D characterisation of fruit trees. Biosyst Eng. 2016;151:479-94.

49. Mammarella M, Comba L, Biglia A, Dabbene F, Gay P. Cooperation of unmanned systems for agricultural applications: A case study in a vineyard. Biosyst Eng. 2022;223:81-102.

50. Mammarella M, Comba L, Biglia A, Dabbene F, Gay P. Cooperation of unmanned systems for agricultural applications: A theoretical framework. Biosyst Eng. 2022;223:61-80.

51. Potena C, Khanna R, Nieto J, Siegwart R, Nardi D, Pretto A. AgriColMap: Aerial-ground collaborative 3D mapping for precision farming. IEEE Robot Autom Lett. 2019;4:1085-92.

© 2025 The Author(s). | Published by Agro Intelligence Research Press

52. Tagarakis AC, Filippou E, Kalaitzidis D, Benos L, Busato P, Bochtis D. Proposing UGV and UAV systems for 3D mapping of orchard environments. Sensors. 2022;22:1571.

53. Pretto A, Aravecchia S, Burgard W, Chebrolu N, Dornhege C, Falck T, et al. Building an aerial–ground robotics system for precision farming: An adaptable solution. IEEE Robot Autom Mag. 2020;28:29-49.

54. Zhang C, Mouton C, Valente J, Kooistra L, van Ooteghem R, de Hoog D, et al. Automatic flower cluster estimation in apple orchards using aerial and ground based point clouds. Biosyst Eng. 2022;221:164-80.

55. Briglia N, Williams K, Wu D, Li Y, Tao S, Corke F, et al. Image-based assessment of drought response in grapevines. Front Plant Sci. 2020;11:595.

56. Rossi R, Costafreda-Aumedes S, Leolini L, Leolini C, Bindi M, Moriondo M. Implementation of an algorithm for automated phenotyping through plant 3D-modeling: A practical application on the early detection of water stress. Comput Electron Agric. 2022;197:106937.

57. Scholander PF, Hammel H, Hemmingsen E, Bradstreet E. Hydrostatic pressure and osmotic potential in leaves of mangroves and some other plants. Proc Natl Acad Sci. 1964;52:119-25.

58. Giovos R, Tassopoulos D, Kalivas D, Lougkos N, Priovolou A. Remote sensing vegetation indices in viticulture: A critical review. Agriculture. 2021;11:457.

59. Labbé M, Michaud F. RTAB-Map as an open-source LiDAR and visual simultaneous localization and mapping library for large-scale and long-term online operation. J Field Robot. 2019;36:416-46.

60. Rusu RB, Marton ZC, Blodow N, Dolha M, Beetz M. Towards 3D point cloud based object maps for household environments. Robot Auton Syst. 2008;56:927-41.

61. Zhang W, Qi J, Wan P, Wang H, Xie D, Wang X, et al. An easy-to-use airborne LiDAR data filtering method based on cloth simulation. Remote Sens. 2016;8:501.

62. Edelsbrunner H, Kirkpatrick D, Seidel R. On the shape of a set of points in the plane. IEEE Trans Inf Theory. 1983;29:551-9.

63. Álvarez S, Sánchez-Blanco MJ. Changes in growth rate, root morphology and water use efficiency of potted Callistemon citrinus plants in response to different levels of water deficit. Sci Hortic. 2013;156:54-62.

64. Lacerda LN, Snider JL, Cohen Y, Liakos V, Gobbo S, Vellidis G. Using UAV-based thermal imagery to detect crop water status variability in cotton. Smart Agric Technol. 2022;2:100029.

65. Polvara R, Molina S, Hroob I, Papadimitriou A, Tsiolis K, Giakoumis D, et al. Bacchus Long-Term (BLT) data set: Acquisition of the agricultural multimodal BLT data set with automated robot deployment. J Field Robot. 2023. https://doi.org/10.1002/rob.22228.

66. Cándido-Mireles M, Hernández-Gama R, Salas J. Detecting vineyard plants stress in situ using deep learning. Comput Electron Agric. 2023;210:107837.

67. Quan L, Jiang W, Li H, Li H, Wang Q, Chen L. Intelligent intra-row robotic weeding system combining deep learning technology with a targeted weeding mode. Biosyst Eng. 2022;216:13-31.

© 2025 The Author(s). | Published by Agro Intelligence Research Press